Journal of Electronics, Electromedical Engineering, and Medical Informatics
Homepage: jeeemi.org; Vol. 8, No. 4, October 2026, pp: 1687-1701 e-ISSN: 2656-8632

RESEARCH ARTICLE OPEN ACCESS

Embedded Colour- and Electrodermal-Based Pressure Injury Staging and Objective Pain Assessment System Powered by a Proton Battery

Wahmisari Priharti[1], Husneni Mukhtar[1], Dien Rahmawati[1], and Nur Hidayah Ahmad[2]

[1] Advanced Biomedical Intelligent Engineering Laboratory, Biomedical & Healthcare Technology Center of Excellence, School of Electrical Engineering, Telkom University, Bandung, Indonesia
[2] Advanced Optical Materials Research Group, Department of Physics, Faculty of Science, Universiti Teknologi Malaysia, Skudai, Malaysia

Corresponding author: W. Priharti (e-mail: wpriharti@telkomuniversity.ac.id), **Author(s) Email**: H. Mukhtar (e-mail: husnenimukhtar@telkomuniversity.ac.id, D. Rahmawati (e-mail: dienrahmawati@telkomuniversity.ac.id), NH. Ahmad (e-mail: nurhidayahahmad@utm.my)

Abstract **Pressure injury is a serious health concern among the elderly and individuals with restricted mobility and is often associated with pain that reduces quality of life. Conventional assessment relies on clinician visual inspection and subjective pain scales, which are difficult to apply to patients with limited communication abilities. Therefore, early identification, accurate stage classification and objective pain assessment are essential for effective clinical intervention. This study develops an embedded pressure injury stage classification and pain assessment system integrating a colour sensor and an electrodermal activity (EDA) sensor with a Rule-Based Decision Tree to classify pressure injuries into four clinical stages, powered by a six-cell 1.5 V proton battery pack as an alternative to conventional lithium-based power sources. The system achieved an overall accuracy, precision, recall, and F1-score of 0.88, 0.89, 0.88, and 0.88, respectively. Skin Conductance Level (SCL) increased progressively from Stage 1 to Stage 3 and decreased at Stage 4, indicating a preliminary physiological pattern associated with injury severity. The battery pack maintained a stable output voltage of 9.1 V at an average current consumption of 279.9 mA, demonstrating its feasibility as an alternative power source. Because the thresholds were derived from 70 annotated Medetec images and validated on only two subjects with four injury sites (40 region-level measurements), the reported metrics should be interpreted as preliminary proof-of-concept rather than definitive clinical validation, and larger studies are needed for clinical confirmation.**

Keywords: **Pressure injury; stage classification; objective pain assessment; Proton battery.**

I. Introduction

Pressure ulcers, also known as bedsores, are localised injuries to the skin and underlying tissues caused by continuous pressure that restricts blood circulation and reduces oxygen and nutrient delivery, so that the tissue becomes ischemic and may progress to necrosis if the pressure is not relieved [1]. They arise most often over bony prominences such as the heels, hips, lower back and buttocks, elbow, shoulder, and back of the head, through tissue deformation caused by sustained compression, shear stress, or both [2]. Their development is strongly associated with immobility, as in prolonged bed rest, wheelchair use, or critical illness [3], and is aggravated by moisture, friction, poor nutrition, and impaired sensory perception [4], characteristics common among the elderly, whose ability, sensory perception, and movement decline with age [5]. Approximately two-thirds of cases occur in patients over 70 years old, and up to 83% of hospitalised patients may develop pressure ulcers within the first five days of admission [6]. Clinically, pressure ulcers are categorized into stages I-IV according to the depth and severity of tissue damage [1], as shown in Fig. 1. The term ulcer, which traditionally refers to an open wound with tissue loss, does not apply to early stages such as Stage I or Deep

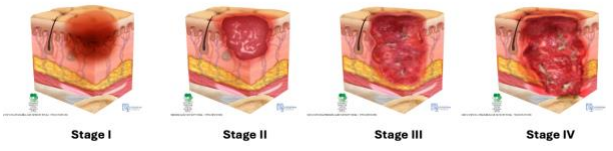


Fig. 1. Clinical stages of pressure injury (Stages 1–4) according to the NPIAP staging system. Reproduced from Revised NPIAP [7]

Manuscript received 7 June 2026; Revised 13 August 2026; Accepted 19 October 2026; Available online 29 October 2026
Digital Object Identifier (**DOI**): https://doi.org/10.35882/jeeemi.v8i4.1828
Copyright © 2026 by the authors. This work is an open-access article and licensed under a Creative Commons Attribution-ShareAlike 4.0 International License (CC BY-SA 4.0)

Tissue Pressure Injury (DTPI), where damage occurs beneath the skin before it becomes visible. Since 2016, the National Pressure Ulcer Advisory Panel (NPUAP) has therefore replaced the term ulcer with injury [7], [8] and renamed itself the National Pressure Injury Advisory Panel (NPIAP), while Roman numerals were replaced by Arabic numerals to avoid confusion with terms such as intravenous (IV). The updated terminology also incorporates current understanding of aetiology, including tissue deformation, impaired perfusion, microclimate effects, nutrition, and tissue tolerance [9], and is used throughout this paper.

Although pressure injuries are recognised as a serious health concern, Indonesia still diagnoses them largely manually, through visual inspection of the affected skin and tools such as the decubitus staging system or the Braden Scale [10]. The Braden Scale assesses six qualitative parameters, namely sensory perception, moisture, activity, mobility, nutrition, and friction/shear, with a score range from 6 to 23 that indicates pressure injury risk [11], [12]. Despite its widespread use, the Braden Scale relies heavily on subjective evaluation and on the patient's ability to perceive and report pain [13], [14]. This is a critical limitation for patients who cannot express pain, such as infants, toddlers, and the elderly, and for those with reduced or absent sensory perception caused by spinal cord injury, neuropathy, diabetes, or prolonged unconsciousness [15], where the lack of reliable sensory feedback can delay detection until the injury is advanced [16].

Therefore, a device is needed to quantitatively identify and classify pressure injuries directly on the body. Most existing studies apply artificial intelligence algorithms to clinical or online pressure injury or database images [17], [18], [19], [20], [21], [22], and several use smartphone-acquired images [23], [24], which introduce variability from camera specifications, lighting and image quality. Furthermore, deep learning classifiers also require substantial computation and are not easily implemented on low-cost microcontrollers. The reported solutions are thus image-dependent, computationally demanding, or restricted to risk prediction, and none couples an objective pain indicator to stage classification at the bedside. This research gap is addressed in the present work.

The present study addresses these limitations with a TCS3200 colour sensor that classifies pressure injury stages from direct colour measurement rather than image analysis, eliminating dependence on camera quality, reducing computational complexity and enabling real-time operation on resource-constrained hardware. An EDA sensor is integrated to detect autonomic responses associated with discomfort or impending tissue injury, even without reported pain, supporting objective assessment and addressing the limitations of the Numeric Rating Scale in individuals with sensory impairment.

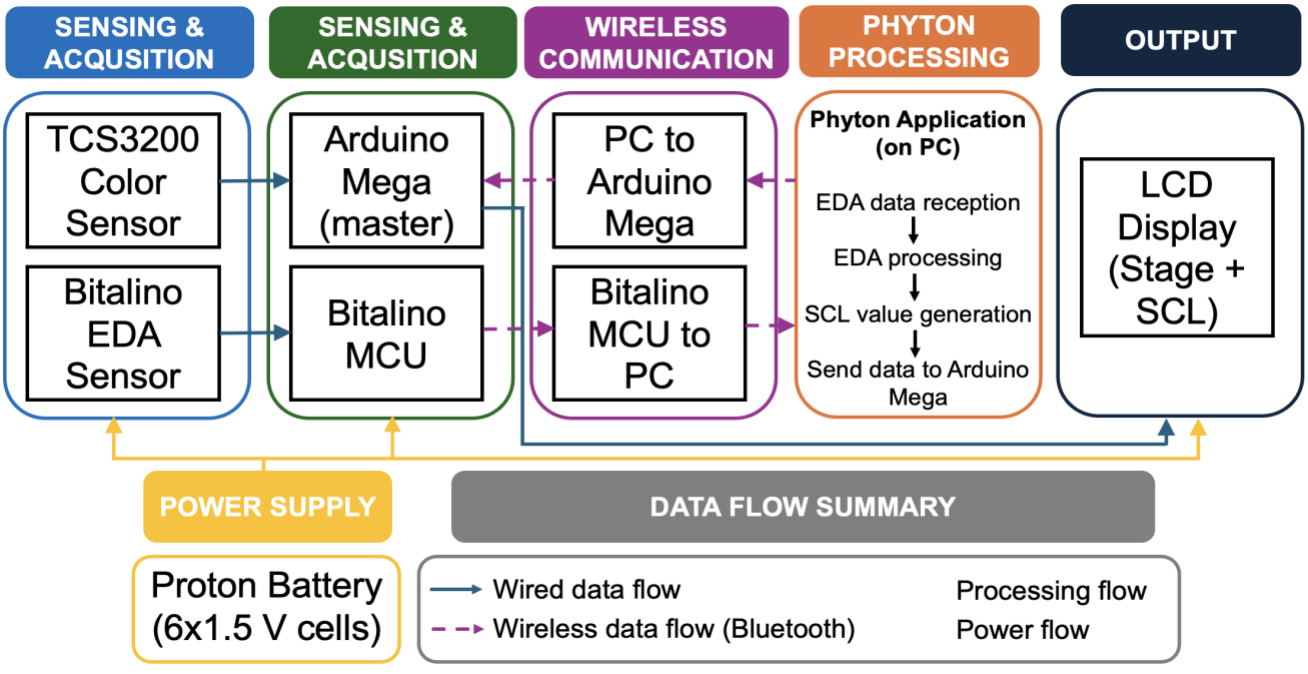


Fig. 2. Block diagram of the proposed embedded pressure-injury assessment system comprising (1) colour-sensor-based stage classification using the TCS3200 and Arduino Mega and (2) EDA-based pain assessment using the BITalino platform.

Manuscript received 7 June 2026; Revised 13 August 2026; Accepted 19 October 2026; Available online 29 October 2026
Digital Object Identifier (**DOI**): https://doi.org/10.35882/jeeemi.v8i4.1828
Copyright © 2026 by the authors. This work is an open-access article and licensed under a Creative Commons Attribution-ShareAlike 4.0 International License (CC BY-SA 4.0)

A portable point-of-care device further requires a compact and safe power source. Lithium-ion (Li-ion) and lithium-polymer (Li-Po) cells dominate portable electronics because of their high energy density and low self-discharge rate, but their non-aqueous, solvent-based electrolytes are prone to leakage and thermal runaway, a fire and explosion hazard in a device used in direct contact with patients [25]. The proton battery, a rechargeable cell using protons (H^+) as charge carriers in an aqueous acidic electrolyte with carbon-based or solid-polymer electrodes, is an emerging alternative [26], [27]. The small ionic radius and low mass of the proton give fast ion-transport even at low temperatures [28], the aqueous electrolyte removes the flammable-solvent hazard [29], and prototypes show acceptable cycle stability [30]. We treat it here as an application-level enabling component rather than an object of electrochemical study.

The novelty of this work lies in integrating three elements within a single embedded, point-of-care device: (i) stage classification obtained directly from TCS3200 colour-sensor readings using a lightweight rule-based decision tree, avoiding the camera dependence and heavy computation of image- and deep-learning-based pipelines; (ii) objective, communication-independent pain assessment through electrodermal activity; and (iii) a proton-battery power supply as a safer alternative to lithium-based chemistries. To the best of our knowledge, this combination has not been reported previously. The aim is therefore to develop and experimentally evaluate a camera-free device that classifies pressure injury into the four NPIAP stages from direct colour measurement while providing an objective pain indicator derived from electrodermal activity, operating entirely from a proton battery. The specific contributions are: (1) a calibrated colour-sensing pipeline in which the raw TCS3200 response is dark- and white-referenced, normalised, and converted through the CIE XYZ and CIE L*a*b* to HSV, making the staging thresholds device- and illumination-independent; (2) per-stage HSV decision ranges derived statistically from 70 annotated Medetec images and encoded as a deterministic rule-based decision tree with an explicit overlap-resolution rule, reported as a numbered algorithm; (3) objective pain assessment from the tonic skin conductance level, integrated in the same device and related to the classified stage; (4) characterisation and integration of a six-cell proton-battrey pack with quantified system-level voltage, current and power; and (5) validation on clinically confirmed pressure injuries under licensed medical supervision, compared systematically with image- and deep-learning-based approaches.

Table 1. Specifications of the principal hardware components used in the proposed pressure-injury staging and EDA-based pain-assessment system.

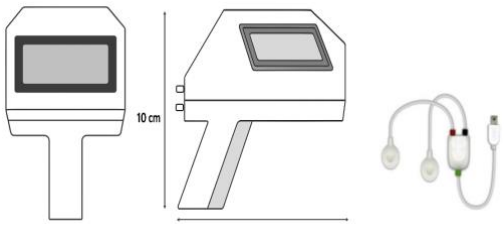
Criteria	Component's name			
	Color sensor	Arduino Mega	EDA[1] Sensor	BITalino MCU[2]
Input voltage (V)	3.3-5	7-12	3.3	3.7 (Li-Po)
Size (mm)	20 × 20	101.5 × 53.3	25 × 15	92 × 60
Sampling Rate (Hz)	10-100	10-1000	1000	Up to 1000
Analog Port	No	16 (A0-A15)	Yes	6 (A0-A5)
Digital Port	Yes	54 (14 PWM)	No	2 (D0, D1)
Required software	Arduino IDE		Open Signals/ Phyton API	

[1)]EDA: Electrodermal Activity; [2)]MCU: Microcontroller Unit

II. Method

A. Hardware Design

The system consists of two sub-systems: (1) stage classification and (2) pain assessment, each with its own microcontroller, namely an Arduino Mega connected to a TCS3200 colour sensor and a BITalino (r)evolution board connected to a BITalino EDA sensor. The EDA signal is analogue and low-voltage and requires amplification, filtering, ADC, and sampling logic provided by the BITalino board, whose 3-pin JST



(a) (b) (c)

Fig. 3. Three-dimensional design of the proposed handheld system: (a) front view, (b) side view, and (c) electrodermal activity (EDA) probe. The enclosure dimensions are approximately 17 cm × 10 cm.

Manuscript received 7 June 2026; Revised 13 August 2026; Accepted 19 October 2026; Available online 29 October 2026
Digital Object Identifier (**DOI**): https://doi.org/10.35882/jeeemi.v8i4.1828
Copyright © 2026 by the authors. This work is an open-access article and licensed under a Creative Commons Attribution-ShareAlike 4.0 International License (CC BY-SA 4.0)

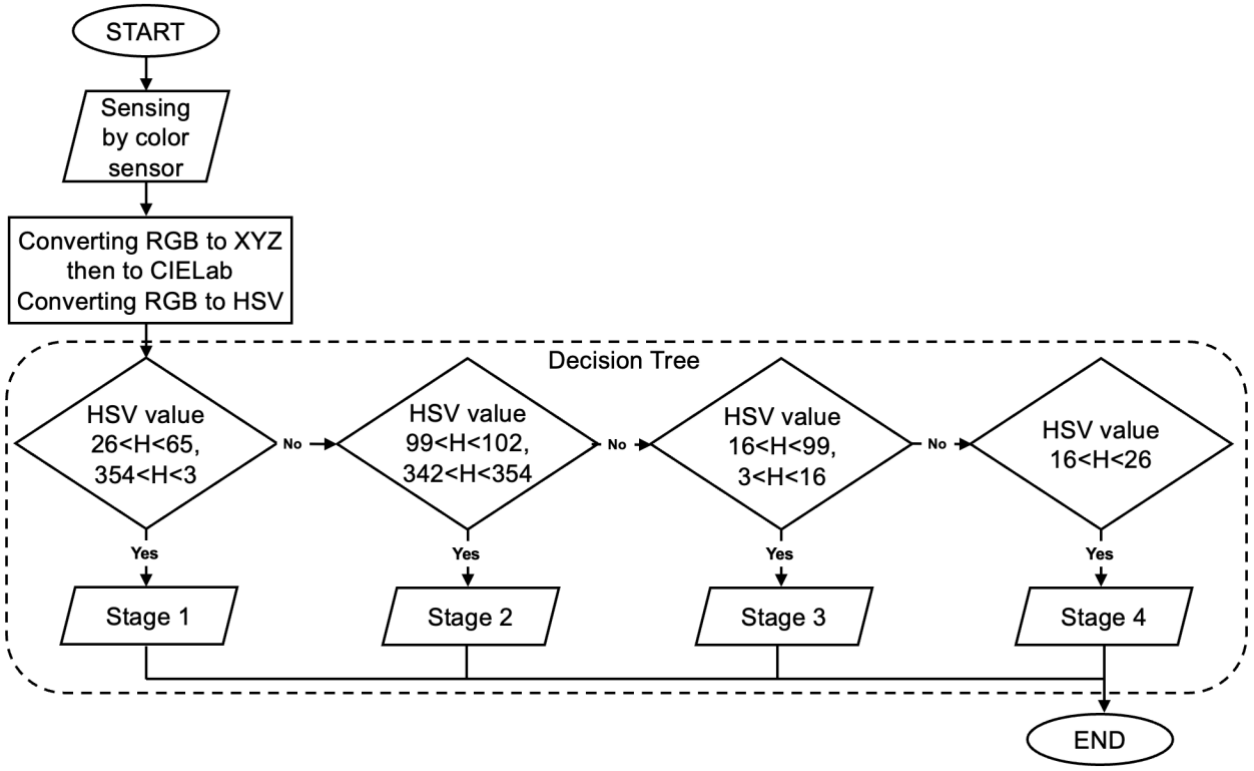


Fig. 4. Flowchart of the rule-based decision tree for classifying pressure injuries into Stages 1–4 using hue, saturation, and value (HSV) colour thresholds derived from the annotated dataset.

connector with custom wiring also does not match Arduino headers; two microcontrollers are therefore needed. The overall process is shown in the block diagram of Fig. 2, and the component specifications are shown in Table 1. The system was designed as a portable handheld device with an additional EDA probe, as shown in Fig. 3, with dimensions of 10 cm high by 17 cm wide side view. A 9V proton battery powers the Arduino and the TCS3200 colour sensor. Although two microcontrollers are used, the classification results are displayed on a single LCD for easier use. The analogue EDA signals are captured by the BITalino microcontroller board and sent to a PC by Bluetooth, analysed with a Python API and returned to the Arduino, which acts as the master microcontroller, classifies the data from both sensors and displays the results on the LCD via I2C.

To determine the stage, the colour sensor was positioned 5-10 mm from the injury under a minimum of 80 lux illumination. For pain assessment, a pre-gelled Ag/AgCl electrode was placed near the injury to measure skin conductivity, which changes with sweat gland activity. The skin was cleaned with 70% isopropyl alcohol (about 2 min), followed by a 3–5-min stabilisation period for skin-electrode equilibrium. Baseline activity was then recorded for 1 min, followed by five stimulus trials of 20-30 s each, giving a session of about 10-15 min. Electrodes were positioned approximately 2 cm from the wound margin on intact skin at a consistent anatomical site per subject. All recordings were made with the subject at rest and before any wound manipulation, at a controlled ambient temperature of 24–26 °C, and each participant's current medication was recorded.

Table 2. Measured output voltage of the evaluated solid biopolymer electrolyte (SBE) formulations.

SAMPLE	Voltage (V)
CMC[1)]+AC[2)]	1.522
CMC+AC+PC[3)]	1.580
CMC+LiOH[4)]	1.581
CMC+LiOH+PC	1.610

[1)]CMC: carboxymethyl cellulose; [2)]AC: Activated Carbon; [3)]PC: pyrolytic carbon; [4)]LiOH: Lithium Hydroxide.

B. Battery Development

A proton battery, also called a solid-state hydrogen cell (SSHC), uses carbon as its main material and can employ plasticized solid polymer-based electrodes made of organic material (solid biopolymer electrode, SBE). The SBE was developed primarily from carboxymethyl cellulose (CMC), whose hydrophilic properties facilitate proton transport pathways and reduce interfacial resistance. Activated Carbon (AC) is

Manuscript received 7 June 2026; Revised 13 August 2026; Accepted 19 October 2026; Available online 29 October 2026
Digital Object Identifier (**DOI**): https://doi.org/10.35882/jeeemi.v8i4.1828
Copyright © 2026 by the authors. This work is an open-access article and licensed under a Creative Commons Attribution-ShareAlike 4.0 International License (CC BY-SA 4.0)

the primary electron-conducting filler and secondary pore-forming agent, Lithium Hydroxide (LiOH) is a solid-state alkaline additive, and pyrolytic carbon (PC) minimises parasitic side reactions and reduces the overpotential of proton intercalation/ desorption [31]. To evaluate the individual and combined contributions of the binder chemistry and the carbon additive, four configurations were prepared from a two-variable factorial design: (1) CMC+AC, (2) CMC+AC+PC, (3) CMC+LiOH, and (4) CMC+LiOH+PC. Configuration (4) yielded the highest and most stable voltage at 1,610 V, as shown in Table 2. The proton battery used in this system follows the 1,5 V Type C (R14) format with dimensions of 26.2×50 mm^2. The fabrication details are described elsewhere [32]. The embedded system requires a supply voltage between 7 V and 9 V, whereas a single fabricated cell delivers a nominal open-circuit voltage of only about 1.5-1.6 V, so six cells were connected in series. For a series string, the terminal voltage of the pack under a load current equals the sum of the individual cell voltages reduced by the drop across the total internal resistance, as expressed in Eq. (1) [33].

$$V_{pack} = \sum_{i=1}^{N_c} V_i - I \sum_{i=1}^{N_c} R_{int,i} \quad (1)$$

where V_{pack} (V) is the terminal voltage of the assembled pack, V_i (V) is the open-circuit voltage of the i-th cell, $R_{int,i}$ (Ω) is the internal resistance of the i-th cell, I (A) is the current drawn by the load, and Nc = 6 is the number of series-connected cells. Under open-circuit conditions (I = 0 A), Eq. (1) reduces to the sum of the individual cell voltages, which is the quantity reported for the assembled pack in the Results section. The electrical demand that the complete prototype imposes on the pack was quantified from the mean measured pack voltage and the mean measured load current. The average power consumption and the energy delivered by the pack over the operating interval were determined using Eq. (2) [33].

$$\bar{P} = \bar{V}_{pack} \cdot \bar{I}, E = \bar{P} \cdot \bar{t}_{op} \quad (2)$$

where $\bar{P}(W)$is the average power consumption of the complete system, $\bar{V}_{pack}$ (V) and $\bar{I}$ (A) are the mean measured pack voltage and mean load current, respectively, $E\ (J)$ is the energy delivered by the pack, and t_{op} (s) is the operating time. Eq. (2) is applied in the Results section to the measured pack voltage and system current.

Table 3. Hue, saturation, and value (HSV) decision ranges for pressure-injury Stages 1–4 derived from 70 annotated Medetec images. The asterisk indicates hue intervals crossing the 0°/360° boundary.

Stage	Hue (deg)	Saturation (%)	Value (%)
Stage 1	354-65.4*	8.0-58.2	60.8-100
Stage 2	342-102*	16.0-82.4	74.9-100
Stage 3	3.1-98.9	17.4-44.8	75.7-96.1
Stage 4	16.4-25.6	39.1-50.2	69.4-73.3

C. Software Design

Pressure injury stage classification is based on the TCS3200 colour sensor, which determines colour from the intensity of red, green, and blue light reflected from a surface through an array of filtered photodiodes. Because the raw output is device- and illumination-dependent, it is calibrated in three steps (dark-offset removal, white-reference scaling and linear colour correction) and then transformed to the XYZ for a device-independent representation, to CIELAB for perceptual uniformity, and finally to HSV. The full calibration and conversion procedure, Eqs. (S1)–(S16) with Fig. S1, is given in the Supplementary Material. Calibration was accepted only when the mean colour difference against the reference patches satisfied dE*ab ≤ 5. The converted HSV value serves as input to the pressure injury stage classification. Using the Rule-Based Decision Tree method, an algorithm based on HSV values was developed to classify pressure injury into four stages. The value for each stage is explained in the system flowchart in Fig. 4.

Table 3 shows HSV decision ranges per stage (centre-region sampling) used by the rule-based decision tree, with hue in degrees (0-360) and saturation and value in %. Ranges marked * wrap across the 0/360 deg boundary. The thresholds were obtained from the center region of each annotated image and applied without modification during patient validation, ensuring an independent evaluation of the decision rules. A total of 70 annotated pressure injury images from the Medetec database were used,

Table 4. Stage-wise classification performance of the rule-based decision tree on 40 region-level clinical measurements.

Stage	TP[1]	FP[1]	FN[1]	Precision[2]	Recall[2]	Specifi city[2]	F1-sco re[2]
Stage 1	8	2	2	80.0	80.0	93.3	80.0
Stage 2	10	0	0	100	100	100	100
Stage 3	9	2	1	81.8	90.0	93.3	85.7
Stage 4	8	1	2	88.9	80.0	96.7	84.2

[1] *TP: True Positive, FP: False Positive, FN: False Negative*
[2] *Precision, recall, specificity, and F1-score are expressed as percentages*

Manuscript received 7 June 2026; Revised 13 August 2026; Accepted 19 October 2026; Available online 29 October 2026
Digital Object Identifier (**DOI**): https://doi.org/10.35882/jeeemi.v8i4.1828
Copyright © 2026 by the authors. This work is an open-access article and licensed under a Creative Commons Attribution-ShareAlike 4.0 International License (CC BY-SA 4.0)

comprising Stage 1 (n = 10), Stage 2 (n = 20), Stage 3 (n = 25), and Stage 4 (n = 15), selected to show clearly visible, unobstructed wound beds. Two representative points, at the edge and centre of the injury, were annotated per image against the Medetec reference staging. These images were used exclusively for rule derivation and threshold determination, after standardisation comprising controlled illumination at 80 lux, white reference calibration, brightness normalisation and colour correction against a reference patch. The Medetec collection predominantly contains lighter skin tones, so generalizability to darker

Table 5. Stage-wise classification outcomes and electrodermal pain-assessment measurements of the proposed embedded system.

Stage	True[1]	False[1]	SCL ± SD[2] (μS)	NRS[3] scale
Stage 1	8	2	152.83±1.42	3
Stage 2	10	0	593.92±2.62	5
Stage 3	9	1	1019.97±0.24	10
Stage 4	8	2	0.3±0.03	N/A[3]

[1]"True" and "False" indicate correct and incorrect stage classifications, respectively.
[2]SCL: skin conductance level; SD: standard deviation.
[3]NRS: Numeric Rating Scale; N/A: not applicable.

pigmentation was not established here and is acknowledged as a limitation. The decision ranges listed in Table 4 were obtained statistically from the annotated dataset rather than being chosen heuristically. Hue, however, is an angular quantity defined on [0°, 360°), so its central tendency cannot be obtained with the ordinary arithmetic mean. The circular mean of Eq. (3) was used instead [34].

$$\bar{H}_s = arctan2\left(\sum_{i\in\omega_s} sinH_i, \sum_{i\in\omega_s} cosH_i\right) mod\ 360° \quad (3)$$

where H_i (deg) is the hue of the i-th annotated sample, Ωs is the set of annotated samples belonging to stage s, arctan2() is the four-quadrant inverse tangent, and $\bar{H}_s$ (deg) is the mean hue of stage s. The modulo operation returns the result to the interval [0°, 360°). This circular treatment is also what produces the two ranges marked with an asterisk in Table 3, which wrap across the 0°/360° boundary. For each stage s and each channel c ∈ {H, S, V}, the decision interval was then defined as the sample mean plus or minus k standard deviations, Eq. (4), with k = 2, so that the interval covers approximately 95% of the annotated observations of that stage under a normal approximation [35]. For hue, the deviations were measured with respect to the circular mean of Eq. (5).

$$T_{s,c}^{min} = \mu_{s,c} - k\sigma_{s,c}, T_{s,c}^{max} = \mu_{s,c} + k\sigma_{s,c} \quad (4)$$

where $\mu_{s,c}$ and $\sigma_{s,c}$ are the sample mean and sample standard deviation of channel c over the annotated samples of stage s, k is the coverage factor, and $T_{s,c}^{min}$ and $T_{s,c}^{max}$ are the lower and upper decision limits that define the hue, saturation and value intervals of stage s reported in Table 3.

$$I_s(H,S,V) = \chi_{Hs}(H) \cdot \chi_{Ss}(S) \cdot \chi_{Vs}(V) \quad (5)$$

where $\chi_{Xx}(X)$ is the indicator function, equal to 1 when x lies inside the interval X and 0 otherwise, and I_s(H, S, V) ∈ {0, 1} is the membership indicator of stage s. The candidate set is defined as A = {s : Is(H, S, V) = 1}. Because the hue intervals of adjacent stages overlap (Table 3), the candidate set A may contain more than one stage. The ambiguity is resolved deterministically by assigning the measurement to the candidate stage whose circular mean hue is closest to the measured hue, Eq. (6); if A is empty, the measurement is reported as unclassified instead of being forced into a stage [34], [35].

$$\hat{s} = \arg min \Delta_c(H, \bar{H}), \quad \Delta_c(\alpha,\beta) = min(|\alpha-\beta|, 360° - |\alpha-\beta|) \quad (6)$$

where ŝ is the predicted stage, Δc(α, β) is the circular distance between two angles expressed in degrees, and |·| denotes the absolute value. This rule guarantees a unique output for every measurement and is the only tie-breaking mechanism used by the classifier. The complete procedure, from the offline derivation of the thresholds to embedded classification, electrodermal processing and presentation of the result, is summarised in Algorithm S1 in the Supplementary Material. Lines 1-18 are executed once on a workstation and produce the twelve threshold constants of Table 3. Lines 19-39 are the procedure that runs on the device itself. Lines 28-30 state explicitly how a reading that falls inside the ranges of more than one stage is resolved, and how a reading that matches no stage is reported.

Validation was conducted on two subjects with clinically confirmed pressure injuries under the supervision of licensed medical personnel, with reference staging, injury location, characteristics and clinical background established beforehand (details and EDA electrode positions are given in Table S1 in the Supplementary Material). The system was deployed in the subjects' homes under controlled illumination (80 lux). Ten injury regions (edge and centre) were sampled, producing 40 observations, while the EDA sensor near the injury recorded five averaged values per injury. The deterministic rule-based decision tree derived from the Medetec dataset was applied without parameter modification to ensure independent evaluation. Its threshold-based structure requires minimal computational resources and enables real-time execution on embedded hardware. Performance was assessed at the image-region level using a confusion matrix comparing predicted and reference labels, from which accuracy, precision,

Manuscript received 7 June 2026; Revised 13 August 2026; Accepted 19 October 2026; Available online 29 October 2026
Digital Object Identifier (**DOI**): https://doi.org/10.35882/jeeemi.v8i4.1828
Copyright © 2026 by the authors. This work is an open-access article and licensed under a Creative Commons Attribution-ShareAlike 4.0 International License (CC BY-SA 4.0)

recall, and F1-score were calculated using Eqs. (7)-(10).

$$\text{Accuracy} = \frac{TP + TN}{TP + TN + FP + FN} \quad (7)$$

$$\text{Precision} = \frac{TP}{TP + FP} \quad (8)$$

$$Recall = \frac{TP}{TP + FN} \quad (9)$$

$$F1\ score = 2 \times \frac{Precision \times Recall}{Precision + Recall} \quad (10)$$

where TP represents the number of samples correctly classified as positive, TN represents the number of samples correctly classified as negative, FP represents the number of negative samples incorrectly classified as positive, and FN represents the number of positive samples incorrectly classified as negative. Accuracy indicates the proportion of correctly classified samples among all samples, precision measures the proportion of correctly predicted positive samples among all samples predicted as positive, recall measures the proportion of actual positive samples that are correctly identified, and the F1-score represents the harmonic mean of precision and recall. Because the clinical validation set is small, every proportion is reported together with a 95% confidence interval computed with the Wilson score method, which remains valid for small samples and for proportions close to 0 or 1, the expression is given in the Supplementary Material.

D. Electrodermal Activity (EDA) Measurement for Pain Assessment

One of the most used methods for assessing pain is the Numeric Rating Scale (NRS) [36], which rates pain from 0 to 10 as no pain (0), mild (1-3), moderate (4-6), and severe (7-10). It has good reliability, validity and responsiveness and requires no special equipment, but it is subjective and depends on the patient's cognition and communication. In patients who may not feel pain because of neuropathy, spinal cord injury or limited sensory perception, the NRS cannot detect underlying physiological changes until the patient feels and reports pain. Electrodermal Activity (EDA) is a biomarker that reflects an individual's responsiveness to stimuli, including pain, and is a useful pain indicator in clinical settings. It works by placing two electrodes on the skin and measuring the skin's conductivity as nerve-mediated sweating changes the sweat excreted by the sweat glands [37]. The electrical conductivity produced by the skin (typically expressed in micro-siemens, μS) has two components: tonic activity, the Skin Conductance Level (SCL), which indicates the baseline value of the skin's electrical conductance, and phasic activity, the Skin Conductance Response (SCR), a rapid change triggered by a specific stimulus. When a person experiences pain, skin conductivity increases proportionally as the sweat glands secrete sweat containing water and ionic salts, especially NaCl [38].

The electrodermal signal was acquired with the BITalino EDA sensor, which applies a constant voltage across two Ag/AgCl electrodes and digitises the resulting current with a 10-bit converter at 1000 Hz on channel A3. Each sample is converted to skin conductance through the front-end transfer function and modelled as the superposition of a slowly varying tonic component (SCL) and faster, stimulus-locked phasic responses (SCR) [39]. Because the recordings were acquired continuously without discrete external stimuli, no phasic activity was elicited, and the tonic term dominates, so the value reported for each recording is the mean conductance over the analysis window, with its standard deviation quantifying within-recording variability. The corresponding expressions, Eqs. (S17)-(S19), are given in the Supplementary Material.

The EDA sensor is used here to assess pain in elderly individuals who have difficulty communicating, so that the NRS scale is limited or unavailable (N/A). More accurate pain assessment would require additional modalities such as heart rate, respiratory rate and blood pressure, which should be used alongside it. Due to some limitations, these were not available in this study. The objective was therefore to measure skin conductance and compare it with the NRS scale to obtain baseline data. Every reported quantity is affected by random and systematic effects, combined following the standard approach for the expression of uncertainty in measurement [40]. The Type A component was evaluated statistically as the standard deviation of the mean of the repeated readings, and the Type B component from the resolution and accuracy specifications of the instruments used, namely the digital multimeter, the quantisation step of the colour channels and the least significant bit of the 10-bit electrodermal converter, the two being combined and expanded as in Eq. (11) [40].

$$u_C = \sqrt{u_A^2 + u_B^2},\ U = k \cdot u_C \quad (11)$$

where u_A is the Type A (statistical) standard uncertainty, u_B is the Type B (instrumental) standard uncertainty, u_C is the combined standard uncertainty, k = 2 is the coverage factor corresponding to an approximate 95% level of confidence, and U is the expanded uncertainty. All tolerances quoted in the Result section were obtained in this way.

III. Result

A. Embedded System Performance

After obtaining the RGB colour range from the Stage 1-4 injury regions, conversion to the CIELAB and HSV colour spaces was performed for both the edge and centre areas, and the resulting HSV ranges were used as input to the Rule-Based Decision Tree. Overall performance was evaluated with a confusion matrix,

Manuscript received 7 June 2026; Revised 13 August 2026; Accepted 19 October 2026; Available online 29 October 2026
Digital Object Identifier (**DOI**): https://doi.org/10.35882/jeeemi.v8i4.1828
Copyright © 2026 by the authors. This work is an open-access article and licensed under a Creative Commons Attribution-ShareAlike 4.0 International License (CC BY-SA 4.0)

from which accuracy, precision, recall, and F1-score were calculated, as presented in Fig. 5.

Table 4 presents class-wise performance derived from the confusion matrix (one-vs-rest; n = 40 region-level measurements, values in %). The overall region-level accuracy was 35/40 = 87.5% (95% Wilson confidence interval 73.9-94.5%). Given the small sample and repeated edge/ center measurements from the same wounds, these intervals are wide and should

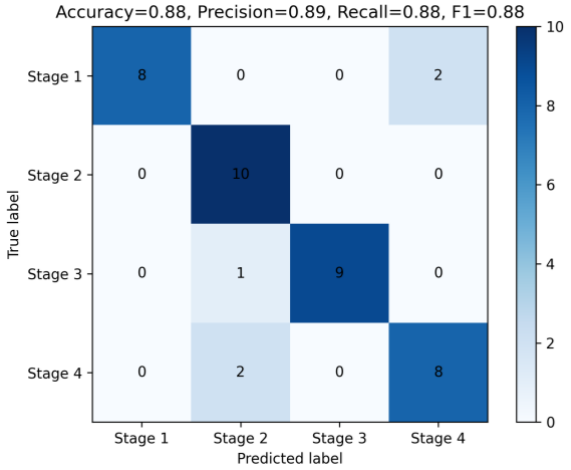


Fig. 5. Confusion matrix of the rule-based pressure-injury stage classifier evaluated on 40 region-level measurements. Rows represent reference stages and columns represent predicted stages; matrix entries indicate the number of observations.

be interpreted with caution. Stage 2 is separated most reliably, whereas Stage 1 shows the lowest precision and recall because its color overlaps with adjacent stages. The individual mean SCL per recording for both patients are reported in Table S2 in the Supplementary Material. The representative per-stage values correspond to the mean stage recordings in Table 5 (Stage 1 = 152.83 ± 1.42, Stage 2 = 593.92 ± 2.62, Stage 3 approx. 1019.97 ± 0.24, Stage 4 = 0.3 ± 0.03). The very low SCL of the Stage 4 patient is consistent with extensive sensory-nerve damage and near-absent electrodermal response. Because SCL is a physiological proxy influenced by several confounders and the sample is small, this relationship is indicative only. The EDA data were acquired continuously without discrete external stimuli, so the recorded EDA signal represents the tonic component of skin conductance, the Skin Conductance Level (SCL), which reflects baseline sympathetic nervous system activity and is appropriate for monitoring sustained physiological conditions such as ongoing pain.

B. Battery Performance

To evaluate the feasibility of the fabricated proton battery as an alternative power source, the electrical characteristics of the individual cells were investigated first. Since the embedded system requires an operating voltage between 7–9 V, six cells were connected in series, and prior to integration, each cell was characterised through repeated open-circuit voltage

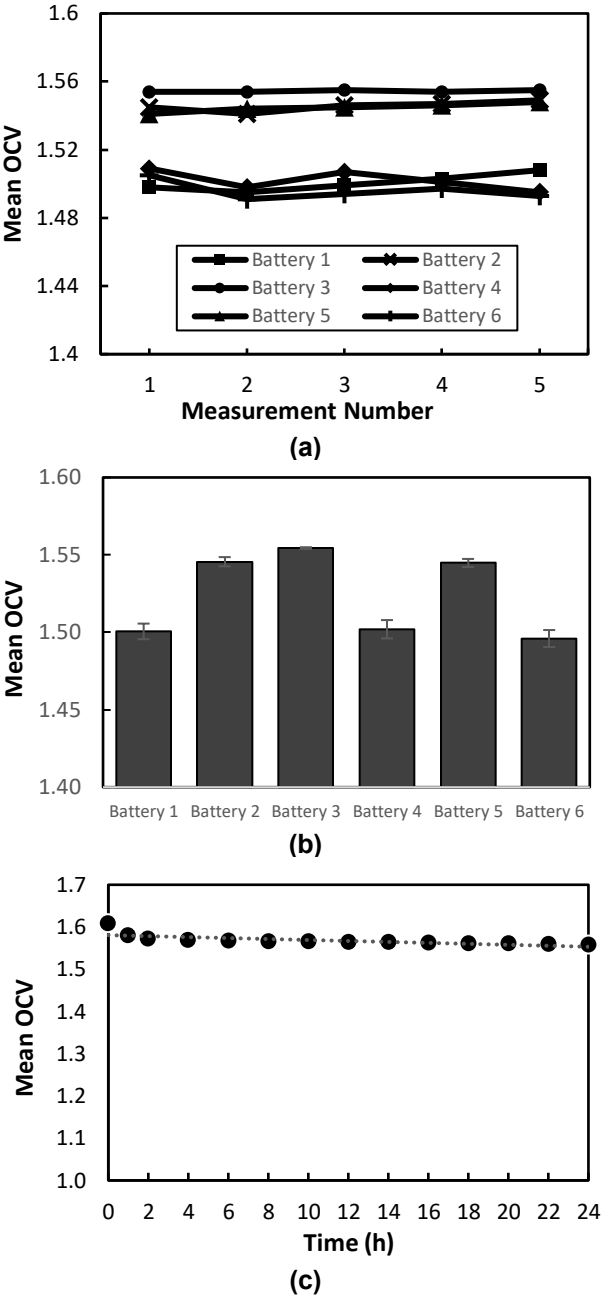


Fig. 6. Electrical performance of the fabricated proton batteries: (a) open-circuit voltage of six individual cells over five repeated measurements, (b) mean open-circuit voltage of each cell, and (c) mean open-circuit voltage stability during 24 h of monitoring.

Manuscript received 7 June 2026; Revised 13 August 2026; Accepted 19 October 2026; Available online 29 October 2026
Digital Object Identifier (**DOI**): https://doi.org/10.35882/jeeemi.v8i4.1828
Copyright © 2026 by the authors. This work is an open-access article and licensed under a Creative Commons Attribution-ShareAlike 4.0 International License (CC BY-SA 4.0)

(OCV) measurements to assess fabrication consistency and voltage stability.

Fig. 6(a) presents the repeated OCV measurements of the six fabricated proton batteries over five trials. The measured voltages remained highly consistent, with Battery 3 exhibiting the highest average voltage of approximately 1.554 ± 0.001 V and Battery 6 the lowest at approximately 1.496 ± 0.005 V. The maximum variation was below 0.01 V, indicating excellent repeatability of the fabricated electrochemical cells. The average OCV of each battery is summarised in Fig. 6(b), ranging from approximately 1.496 ± 0.005 V to 1.554 ± 0.001 V, corresponding to a maximum deviation of only about 3.9% among all cells. Such small variation demonstrates reproducible electrochemical characteristics suitable for constructing a multi-cell battery pack. Long-term voltage stability was evaluated through open-circuit monitoring over 24 hours, as illustrated in Fig. 6(c). The average OCV gradually decreased from approximately 1.61 V immediately after fabrication to approximately 1.56 V after 24 hours, a reduction of approximately 3.1%. After the initial stabilization during the first few hours, the voltage remained nearly constant, suggesting relatively low self-discharge during storage under open-circuit conditions. Following individual cell evaluation, six proton batteries were connected in series to form the power source for the embedded system. The assembled pack produced an average output voltage of approximately 9.1 V, satisfying the operating voltage requirement, and successfully powering the complete embedded hardware throughput functional evaluation, demonstrating the feasibility of the fabricated proton battery as an alternative portable energy source.

IV. Discussion

The system demonstrated promising, clinically interpretable performance across all evaluated stages. As summarised in Table 5, it correctly classified 35 of 40 samples, an overall accuracy of 87.5% with 5 incorrect predictions. Stage 1 gave 8 correct classifications out of 10, with an SCL of 152.83 µS corresponding to an NRS of 3, consistent with the mild pain expected from superficial epidermal involvement. Stage 2 was classified completely, 10 out of 10, with an SCL of 593.92 µS and an NRS of 5, reflecting pain from partial-thickness damage extending into the dermis. Stage 3 gave 9 out of 10 correct, an SCL of 1019.97 µS, and an NRS of 10, indicating severe pain consistent with full-thickness tissue destruction. Stage 4 gave 8 out of 10 correct, an SCL of 0.3 µS and a non-applicable NRS. This near-zero SCL observed in Stage 4 was unexpected and may reflect individual physiological or measurement-related factors rather than injury severity. SCL increased gradually from Stage 1 to Stage 3 and decreased markedly at Stage 4. Because the electrodes were positioned adjacent to, rather than on the wound, the measurement represents the electrodermal response of the surrounding skin. EDA primarily reflects sympathetic sudomotor activity through changes in sweat gland activity and skin conductance, and previous studies report EDA changes in response to painful stimuli [41]. Thus, the increase from Stage 1 to Stage 3 may indicate an elevated autonomic response associated with pain or the physiological stress of the injury. The near-zero SCL at Stage 4 cannot, however, be attributed directly to nerve destruction within the wound. Although Stage 4 injuries involve extensive tissue loss that may reach deeper structures [7], the present data are insufficient to establish a direct stage-SCL relationship, and the reduction may also reflect individual physiological variation and measurement factors such as electrode contact, skin hydration, temperature and electrode position. The pattern is therefore preliminary, and studies with more subjects, controlled electrode placement and repeated measurements are needed to confirm reproducibility.

The gradual increase in SCL from Stage 1 to Stage 3 is consistent with Sugimine et al. [42] and Kyriacou et al. [43], who showed that normalised SCL correlates significantly with subjective pain scores, with SCL during physical pain stimulation substantially greater than during general stress not involving pain, supporting SCL as a pain-specific signal. It must be emphasised that SCL is a physiological proxy rather than a direct measure of pain intensity, and because EDA is modulated by sweating, ambient temperature, anxiety, hydration, medication, and emotional state, the present SCL-pain association requires multimodal confirmation. The confusion matrix in Fig. 5 further elaborates the classification behaviour. The model achieved 88% accuracy, 89% precision, 88% recall and an F1-score of 88%, and its diagonal dominance indicates that most samples were assigned correctly, except for Stages 1 and 4, which each accounted for 2 misclassifications. The high F1-score indicates the good classifyication of both positive and negative cases, which matters clinically because incorrect staging directly affects treatment decisions. The primary objective of this study is the development of the embedded classification and pain assessment system rather than the electrochemical optimisation of proton batteries, so battery evaluation focused on electrical consistency and successful system integration instead of comprehensive battery characterisation.

The repeated OCV measurements shown in Fig. 6(a) and Fig. 6(b) demonstrate excellent reproducibility, with very small variations between repeated measurements and among cells. This consistency matters for series-connected packs because voltage imbalance can accelerate capacity degradation and reduce pack reliability. The observed variation of less

Manuscript received 7 June 2026; Revised 13 August 2026; Accepted 19 October 2026; Available online 29 October 2026
Digital Object Identifier (**DOI**): https://doi.org/10.35882/jeeemi.v8i4.1828
Copyright © 2026 by the authors. This work is an open-access article and licensed under a Creative Commons Attribution-ShareAlike 4.0 International License (CC BY-SA 4.0)

Table 6. Systematic comparison of the proposed system with representative pressure injury assessment studies. Metric types are stated explicitly because accuracy and mAP are not comparable quantities.

Study, year [Ref]	Sensing modality & Algorithm/ model	Dataset size	Subjects / clinical cases	Reported performance and error (metric type)	Computational requirement	Validation design
Silva et al., 2021 [17]	Electronic health records & Random Forest	Retrospective ICU records; size not reported	ICU inpatients; count not reported	Accuracy 96%, error 4% (accuracy; risk prediction)	Server-side model on tabular data	Retrospective internal validation
Lau et al., 2022 [24]	Smartphone RGB camera & YOLOv4, TensorFlow Lite on Android	190 original images from Medetec and other public sources; 1,278 training and 144 validation images	None for training or validation; 10 printed test images applied to a forearm	Accuracy 63.2%, error 36.8% (accuracy, 5 classes); 80-90% in the printed real-life test	GPU (CUDA/cuDNN) for training; smartphone for inference	Source-disjoint random split, 10-fold cross-validation, plus a deployment test with three phones at 125 and 58 lux
Aldughayfiq et al., 2023 [18]	RGB clinical photographs & YOLOv5 (detection and classification)	More than 1,000 images (Medetec plus about 200 web images, augmented); 5 classes	None (image-only study)	mAP@50 76.9%, mAP@50-95 39.8%, precision 78.1%, recall 68.5%, F1 73.2% (detection metrics)	Cloud GPU (Google Colab)	Held-out validation set; split ratio not reported
Chang et al., 2024 [23]	Smartphone RGB camera & YOLOv8m, on-device inference	2,800 annotated images; 6 severity classes	None (image-only study)	Accuracy 84.6%, error 15.4%, and mAP@50 90.8% for the same model	GPU for training; mobile inference of about 3 s per image	Train/test on the annotated image set; no patient-level validation reported
Asare-Baiden et al., 2024 [19]	Infrared thermography and optical imaging & CNN (three architectures compared)	Images acquired from 35 participants across a range of skin tones	35 participants; temperature differences induced by cooling and cupping	Accuracy about 88%, error about 12% (accuracy)	GPU	Robustness assessed across cameras, lighting, pose and distance
Liu et al., 2025 [20]	Clinical photographs & Deep-learning segmentation network	Images collected in four hospitals; count not reported	Hospital patients; count not reported	Accuracy about 83%	GPU	Agreement with manual wound count, dimension and area
Priharti et al. [22], 2025	Raspberry Pi camera & CNN	Image dataset; count not reported	Not reported	Accuracy 83.3%, error 16.7% (accuracy)	Raspberry Pi single-board computer	Internal test set
This work, 2025	Non-imaging TCS3200 colour sensor and EDA sensor & Rule-based decision tree	70 annotated Medetec images (140 sampling points), used only to derive the thresholds	2 patients, 4 clinically confirmed injury sites, 40 region-level measurements	Accuracy 87.5% (95% Wilson CI 73.9-94.5%), error 12.5% (5 of 40); precision 89%, recall 88%, F1 88%	8-bit microcontroller, no GPU, deterministic real-time execution	Thresholds derived offline from Medetec and applied without modification

Manuscript received 7 June 2026; Revised 13 August 2026; Accepted 19 October 2026; Available online 29 October 2026
Digital Object Identifier (**DOI**): https://doi.org/10.35882/jeeemi.v8i4.1828
Copyright © 2026 by the authors. This work is an open-access article and licensed under a Creative Commons Attribution-ShareAlike 4.0 International License (CC BY-SA 4.0)

sufficiently uniform electrolyte composition and electrode preparation.

The OCV stability in Fig. 6(c) further indicates favourable electrochemical stability during storage. The initial decrease over the first several hours is consistent with the relaxation behaviour reported for aqueous zinc-based proton batteries, after which the cell voltage remained relatively stable over the remainder of the 24-hour observation, suggesting low self-discharge and suitability for intermittent operation of portable embedded systems. These findings agree with previous electrochemical characterisation of a rechargeable proton battery using the same CMC-LiOH-PC solid biopolymer electrolyte, which achieved an initial OCV of approximately 1.61 V, ionic conductivity of approximately 1.01×10^{-2} S/cm, and an initial discharge capacity of approximately 2.7 mAh at 9 mA, remaining rechargeable over approximately 9-10 cycles before gradual capacity degradation [25], [44]. The close agreement with the voltage obtained here provides additional evidence of comparable electrochemical behaviour despite the different application contexts. Unlike the study, the present work evaluates the proton battery under practical embedded-system operation rather than laboratory battery testing. The assembled six-cell pack provided approximately 9.1 V, enabling continuous operation of the prototype without an external laboratory supply. The measured system current of approximately 280 mA is determined primarily by the combined consumption of the Arduino Mega, BITalino board, TCS3200 sensor, LCD and peripheral circuitry rather than by the intrinsic discharge capability of an individual cell, so the pack demonstrates application feasibility rather than a complete electrochemical evaluation.

During validation, the pack powered the prototype for several hours of continuous measurements and remained operational for up to several days of intermittent use. Because the electrochemical characteristics were not evaluated under controlled constant-current loading, no capacity or runtime is derived theoretically. Future work will include constant-load discharge curves, energy-capacity determination, discharge curves, internal resistance, cycle life, coulombic efficiency and direct comparisons with commercial Li-ion and Li-Po batteries under identical conditions. To position the proposed system relative to existing work, Table 6 compares seven representative studies across sensing modality, algorithm or model, dataset size, subjects or clinical cases, reported performance, computational requirement, and validation design. The studies address different aspects of pressure-injury assessment. Silva et al. [17] focused on pressure-injury risk prediction from electronic health records using random forest and logistic regression, rather than staging existing injuries. Lau et al. [24] investigated smartphone-based RGB imaging with YOLOv4 and TensorFlow Lite, including a deployment test under different lighting conditions. Aldughayfiq et al. [18] developed a YOLOv5-based approach for image detection and classification, while Chang et al. [23] extended smartphone-based assessment using YOLOv8m with on-device inference across six severity classes. Asare-Baiden et al. [19] explored infrared thermography combined with optical imaging and examined robustness across skin tones and imaging conditions, although the experimental conditions did not involve clinically confirmed pressure injuries. Liu et al. [20] addressed wound segmentation from clinical photographs, focusing on quantitative wound delineation rather than direct severity classification. Priharti et al. [22] demonstrated an embedded image-based classification approach using a Raspberry Pi camera and CNN. In contrast, the present work uses non-imaging colour and electrodermal activity sensing with a rule-based decision tree implemented on an 8-bit microcontroller. Thus, the studies share the objective of supporting automated or quantitative pressure-injury assessment but differ in their sensing modality, assessment target, computational architecture, and degree of clinical validation.

Four observations follow from this comparison. First, dataset size and subject count are largely decoupled in this field. The studies with the largest image sets [18], [23] involved no participants, whereas those that did used small cohorts [19], [24]. The present work used 70 annotated images solely to derive thresholds and validated on 40 region-level measurements from two patients, so its validation is genuinely clinical but clearly underpowered, which is why the accuracy is reported with its 95% Wilson interval of 73.9-94.5%. Second, the reported figures measure different quantities. The 76.9% in [18] is a mean average precision at an intersection-over-union threshold of 0.50, a detection metric that also penalises localisation error, whereas the 87.5% obtained here is an accuracy on operator-delimited wound regions and is comparable only with the accuracy entries, being on a par with [23] and [19], higher than [24], and lower than [17], which predicts injury incidence from electronic health records rather than staging an existing injury. Third, the computational requirements differ by orders of magnitude. Every image-based approach requires GPU training, and the on-device implementations still need a smartphone-class processor, whereas the proposed classifier consists of twelve thresholds and a single tie-breaking comparison, Eqs. (4)-(6), runs deterministically on an 8-bit microcontroller and draws 279.9 mA at 9.1 V, about 2.5 W by Eq. (2), although it localizes nothing and stages only the region on which the operator places the probe. Fourth, the validation designs are not equivalent. Most comparable studies evaluate a model on a held-out subset of the same

Manuscript received 7 June 2026; Revised 13 August 2026; Accepted 19 October 2026; Available online 29 October 2026
Digital Object Identifier (**DOI**): https://doi.org/10.35882/jeeemi.v8i4.1828
Copyright © 2026 by the authors. This work is an open-access article and licensed under a Creative Commons Attribution-ShareAlike 4.0 International License (CC BY-SA 4.0)

image collection, whereas here we derived the thresholds from the Medetec and applied them without modification to measurements from a different sensing device, a stricter form of transfer but on a much smaller validation set. The comparison should therefore be interpreted in terms of the different operating regimes and validation contexts of the respective approaches rather than as a direct performance ranking.

Despite the encouraging results, this study is a preliminary proof-of-concept evaluation with several limitations. First, clinical validation was limited to two subjects with four injury sites; the 40 region-level observations are repeated measurements (edge and centre) from the same injuries and do not represent independent clinical cases, which may give an optimistic estimate of performance and widen the true confidence intervals. Second, colour-based staging can be affected by skin tone, infection, moisture, lighting, necrotic tissue and wound-dressing condition, so reliable separation of the four stages by colour alone is not guaranteed across all clinical presentations. Third, SCL is a physiological proxy, not a direct measure of pain intensity, and is influenced by numerous confounders, so multimodal validation is required before it can serve as a quantitative pain indicator. Finally, the battery characterisation is limited to OCV repeatability, stability, and successful integration. Full discharge profiling, runtime, energy capacity, rechargeability, cycle life and identical-load comparison against Li-ion/Li-Po cells remain ongoing work. Larger multi-centre studies with independent cases and greater skin-tone diversity are needed to confirm these findings.

V. Conclusion

This study developed and evaluated an embedded pressure injury stage classification and pain assessment system powered by a six-cell proton battery pack as an alternative to conventional lithium-based power sources. The system integrated a colour sensor and an EDA sensor and employed a Rule-Based Decision Tree to classify pressure injuries across four clinical stages, achieving an overall accuracy, precision, recall, and F1-score of 0.88, 0.89, 0.88, and 0.88, respectively, a well-balanced result for preliminary proof-of-concept evaluation. The observed variation in SCL across stages indicates the potential of EDA as a physiological indicator for objective pain assessment, although the increase from Stage 1 to Stage 3 and the subsequent decrease at Stage 4 remain preliminary and do not yet establish a direct relationship between SCL, pain, and injury severity. The proton battery pack maintained a stable output of 9.1 V at an average current consumption of 279.9 mA, demonstrating its viability as a safer clinical power alternative to conventional Li-ion or Li-Po batteries. The proposed system therefore shows strong potential as a practical, energy-efficient tool for real-time pressure injury assessment at the point of care, with future work recommended to expand the dataset for broader clinical validation.

Declarations

Ethical Approval

This study was conducted in accordance with ethical standards and has received approval from the Health Research Ethics Committee, National Research and Innovation Agency, with approval number [032/KE.03/SK/03/2025].

Informed Consent

Informed consent was obtained from all participants or, where applicable, from their legally authorized representatives prior to participation in the study.

Consent for Publication Participants

Consent for publication was obtained from all participants or their legally authorized representatives for the publication of anonymized data and study findings.

Funding

This research received no specific grant from any funding agency in the public, commercial, or not-for-profit sectors.

Author Contribution

- W. Priharti: Conceptualization, Methodology, Investigation, Data Curation, Formal Analysis, and Writing Original Draft, Review and Editing.
- H. Mukhtar and D. Rahmawati: Investigation, Software, Formal Analysis, and Writing Review and Editing.
- N.H. Ahmad: Investigation, Validation, and Writing Review and Editing.

All authors reviewed and approved the final version of the manuscript and agree to be accountable for all aspects of the work, ensuring its integrity and accuracy.

Data Availability

The datasets generated and/or analyzed during the current study are not publicly available because of participant privacy and ethical restrictions but may be obtained from the corresponding author upon reasonable request and subject to ethical approval.

Code Availability

The source code and embedded implementation used in this study are available from the corresponding author upon reasonable request.

Competing Interests

The authors declare no competing interests.

Generative AI Declaration

Manuscript received 7 June 2026; Revised 13 August 2026; Accepted 19 October 2026; Available online 29 October 2026
Digital Object Identifier (**DOI**): https://doi.org/10.35882/jeeemi.v8i4.1828
Copyright © 2026 by the authors. This work is an open-access article and licensed under a Creative Commons Attribution-ShareAlike 4.0 International License (CC BY-SA 4.0)

During preparation of this manuscript, the authors used a generative artificial intelligence tool solely for language refinement and grammatical improvement. The authors subsequently reviewed and edited the output and take full responsibility for the content of the manuscript.

Acknowledgment
The authors would like to express sincere gratitude to the Directorate of Research and Community Service, Telkom University and Universiti Teknologi Malaysia for the invaluable support and resources provided throughout this research. This study would not have been possible without the institution's commitment to advancing research and innovation in biomedical electronics. The authors also gratefully acknowledge Hilmi Hafizh and Mega Alfareza for their valuable assistance with field data collection during this study.

Clinical Trial Registration
Clinical trial registration was not applicable because this study did not involve a prospective interventional clinical trial.

Declaration of Originality
The authors confirm that this manuscript is original, has not been published previously, and is not under consideration for publication elsewhere.

References

[1] S. Bhattacharya and R. K. Mishra, "Pressure ulcers: Current understanding and newer modalities of treatment," *Indian J Plast Surg*, vol. 48, no. 1, pp. 4–16, 2015, doi: 10.4103/0970-0358.155260.

[2] S. R. H. Zaidi and S. Sharma, *Pressure Ulcer*. Treasure Island (FL): StatPearls Publishing, 2025.

[3] E. B. Jaul and M. Calderon-Margalit, "Systemic factors and mortality in elderly patients with pressure ulcers," *Int. Wound J.*, vol. 12, no. 3, pp. 254–259, 2015.

[4] E. Jaul, J. Barron, J. P. Rosenzweig, and et al., "An overview of co-morbidities and the development of pressure ulcers among older adults," *BMC Geriatr*, vol. 18, p. 305, 2018, doi: 10.1186/s12877-018-0997-7.

[5] S. Coleman *et al.*, "Patient risk factors for pressure ulcer development: systematic review," *Int. J. Nurs. Stud.*, vol. 50, no. 7, pp. 974–1003, 2013, doi: 10.1016/j.ijnurstu.2012.11.019.

[6] Z. Razi-Chafi, M. Esmaeilpour-Bandboni, and Z. Salmalian, "Prevalence of pressure ulcer and its related factors in elderly patients hospitalized to teaching hospitals in East Guilan," *JCOMS*, vol. 3, no. 1, pp. 375–381, 2023.

[7] L. E. Edsberg, J. M. Black, M. Goldberg, L. McNichol, L. Moore, and M. Sieggreen, "Revised National Pressure Ulcer Advisory Panel Pressure Injury Staging System," *J. Wound Ostomy Continence Nurs.*, vol. 43, no. 6, pp. 585–597, 2016, doi: 10.1097/WON.0000000000000281.

[8] L. E. Edsberg, J. Cox, K. Koloms, and C. A. VanGilder-Freese, "Implementation of Pressure Injury Prevention Strategies in Acute Care: Results From the 2018-2019 International Pressure Injury Prevalence Survey," *J. Wound Ostomy Continence Nurs.*, vol. 49, no. 3, pp. 211–219, 2022, doi: 10.1097/WON.0000000000000878.

[9] J. M. Black *et al.*, "Pressure ulcers: avoidable or unavoidable? Results of the National Pressure Ulcer Advisory Panel consensus conference," *Ostomy Wound Manage.*, vol. 57, no. 2, pp. 24–37, 2011.

[10] S. Chou and et al., "Predictive Validity of the Braden Scale for Pressure Injury Risk in Different Clinical Settings: A Systematic Review," *Int. J. Nurs. Stud.*, vol. 118, 2021.

[11] S. Gaspar and et al., "Reliability and Validity of the Braden Scale in Older Adults," *J. Wound Care*, vol. 29, no. 12, pp. 713–720, 2020.

[12] Agency for Healthcare Research and Quality, "Pressure Ulcer Prevention and Treatment Protocol," 2020. [Online]. Available: https://www.ahrq.gov/patient-safety/settings/hospital/resource/pressureulcer/tool/pu7b.html

[13] A. Mehicic, A. Burston, and P. Fulbrook, "Psychometric properties of the Braden scale to assess pressure injury risk in intensive care: A systematic review," *Intensive Crit. Care Nurs.*, vol. 83, p. 103686, 2024, doi: 10.1016/j.iccn.2024.103686.

[14] Y. Lyu, Y.-L. Huang, Z.-Y. Li, and F. Lin, "Interventions and strategies to prevent medical device-related pressure injury in adult patients: A systematic review," *J. Clin. Nurs.*, vol. 32, no. 19–20, pp. 6863–6878, 2023, doi: 10.1111/jocn.16790.

[15] S. Fryer, S. Caggiari, D. Major, D. L. Bader, and P. R. Worsley, "Continuous pressure monitoring of inpatient spinal cord injured patients: implications for pressure ulcer development," *Spinal Cord*, vol. 61, pp. 111–118, 2023, doi: 10.1038/s41393-022-00841-7.

[16] A. Burston, S. J. Miles, and P. Fulbrook, "Patient and carer experience of living with a pressure injury: A meta-synthesis of qualitative studies," *J. Clin. Nurs.*, vol. 32, no. 13–14, pp. 3233–3247, 2023, doi: 10.1111/jocn.16431.

[17] H. P. Silva *et al.*, "Prediction of Pressure Injury Incidence in ICU Patients Using Machine Learning," *arXiv preprint arXiv:2112.13687*,

Manuscript received 7 June 2026; Revised 13 August 2026; Accepted 19 October 2026; Available online 29 October 2026
Digital Object Identifier (**DOI**): https://doi.org/10.35882/jeeemi.v8i4.1828
Copyright © 2026 by the authors. This work is an open-access article and licensed under a Creative Commons Attribution-ShareAlike 4.0 International License (CC BY-SA 4.0)

2021, [Online]. Available: https://arxiv.org/abs/2112.13687

[18] B. Aldughayfiq, F. Ashfaq, N. Z. Jhanjhi, and M. Humayun, "YOLO-Based Deep Learning Model for Pressure Ulcer Detection and Classification," *Healthcare*, vol. 11, no. 9, p. 1222, 2023, doi: 10.3390/healthcare11091222.

[19] M. Asare-Baiden *et al.*, "A Feasibility Study of Thermography for Detecting Pressure Injuries Across Diverse Skin Tones," *medRxiv*, p. 2024.10.14.24315465, Oct. 2024, doi: 10.1101/2024.10.14.24315465.

[20] A. Liu *et al.*, "Development of a Deep Learning-Based Model for Pressure Injury Surface Assessment," *J. Clin. Nurs.*, vol. 34, no. 10, pp. 4246–4258, Oct. 2025, doi: https://doi.org/10.1111/jocn.17645.

[21] H. Kzl, A. Ylmaz, M. Demiral, U. Kaya, and R. Çakr, "Evaluation of the Effectiveness of Deep Learning Model in Detection and Classification of Pressure Injury," *Journal of Intensive Care Nursing*, vol. 29, no. 3, pp. 207–219, 2025, doi: 10.62111/ybhd.1749992.

[22] W. Priharti, H. Mukhtar, I. M. P. Giriwara, I. M. A. Majesta, and W. A. B. Bimantara, "Design of Deep Learning-Based Pressure Injury Stage Classification Device," *Jurnal Rekayasa Elektrika*, vol. 21, no. 2, pp. 83–92, Jun. 2025, doi: 10.17529/jre.v21i2.41353.

[23] K.-Y. Chang, C.-H. Lin, and M.-F. Tsai, "Edge-Based Deep Learning System for On-Device Pressure Ulcer Detection Using YOLOv8," *Applied Sciences*, vol. 14, no. 16, p. 7124, 2024, doi: 10.3390/app14167124.

[24] H. Lau, B. So, and K. Lai, "A Smartphone Application for Pressure Injury Assessment Using AI-Based Image Classification," *JMIR Form. Res.*, vol. 6, no. 10, p. e37411, 2022, doi: 10.2196/37411.

[25] M. I. N. Isa, M. I. H. Sohaimy, and N. H. Ahmad, "Carboxymethyl cellulose plasticized polymer application as bio-material in solid-state hydrogen ionic cell," *Int. J. Hydrogen Energy*, vol. 44, no. 16, pp. 8298–8306, 2019, doi: 10.1016/j.ijhydene.2019.01.180.

[26] L. Zhang, C. Zhang, and E. J. Berg, "Mastering Proton Activities in Aqueous Batteries," *Advanced Materials*, vol. 37, no. 23, p. 2407852, Jun. 2025, doi: https://doi.org/10.1002/adma.202407852.

[27] C. Huang, W. Zhang, and W. Zheng, "Proton batteries shape the next energy storage," *Energy Storage Mater.*, vol. 61, p. 102913, 2023, doi: https://doi.org/10.1016/j.ensm.2023.102913.

[28] B. Zhang and others, "Cathode materials for proton batteries: recent advances and perspectives," *J. Mater. Chem. A*, vol. 13, pp. 18183–18208, 2025, doi: 10.1039/D5TA02851E.

[29] Y. Zhong *et al.*, "Design methodology of a promising category of metal phosphate electrodes for quasi-solid-state proton batteries," *Natl. Sci. Rev.*, vol. 12, no. 7, p. nwaf226, Jul. 2025, doi: 10.1093/nsr/nwaf226.

[30] B. Su *et al.*, "Water-in-Acid Strategy for Corrosion-Free Proton Storage: Phosphoric Acid Electrolyte Engineering Toward Sustainable Aqueous Batteries," *Angew. Chem. Int. Ed.*, vol. 64, no. 25, p. e202505769, Jun. 2025, doi: https://doi.org/10.1002/anie.202505769.

[31] M. N. Faeqah, M. I. H. Sohaimy, N. H. Ahmad, M. Muthuvinayagam, and M. I. N. Isa, "Structural study of 2-hydroxyethyl cellulose (2HEC) solid biopolymer electrolyte doped with NH4Br: effect on ionic conductivity," *Ionics (Kiel).*, vol. 31, no. 9, pp. 9133–9145, 2025, doi: 10.1007/s11581-025-06495-8.

[32] N. H. Ahmad, M. N. H. Mahmud, and F. E. Zainuddin, "Carboxymethyl Cellulose Doped Ammonium Iodide Solid Biopolymer Electrolytes: Electrical and Structural Analysis," International Exchange and Innovation Conference on Engineering & Sciences, 2025.

[33] T. B. Reddy, Ed., *Linden's Handbook of Batteries*, 4th ed. New York, NY, USA: McGraw-Hill, 2011.

[34] K. V Mardia and P. E. Jupp, *Directional Statistics*. Chichester, U.K.: Wiley, 2000.

[35] J. Han, M. Kamber, and J. Pei, *Data Mining: Concepts and Techniques*, 3rd ed. Waltham, MA, USA: Morgan Kaufmann, 2012.

[36] O. Karcioglu and others, "A Systematic Review of the Pain Scales in Adults: Which to Use?," *Am. J. Emerg. Med.*, vol. 38, no. 4, pp. 707–714, 2020, doi: 10.1016/j.ajem.2019.09.008.

[37] R. Sánchez-Reolid, F. L. de la Rosa, D. Sánchez-Reolid, M. T. López, and A. Fernández-Caballero, "Machine Learning Techniques for Arousal Classification from Electrodermal Activity: A Systematic Review," *Sensors*, vol. 22, no. 22, p. 8886, 2022, doi: 10.3390/s22228886.

[38] O. N. Rahma, A. P. Putra, A. Rahmatillah, and others, "Electrodermal Activity for Measuring Cognitive and Emotional Stress Level," *J. Med. Signals Sens.*, vol. 12, no. 2, pp. 155–162, 2022, doi: 10.4103/jmss.JMSS_78_20.

[39] M. Benedek and C. Kaernbach, "A continuous measure of phasic electrodermal activity," *J. Neurosci. Methods*, vol. 190, no. 1, pp. 80–91, 2010, doi: 10.1016/j.jneumeth.2010.04.028.

[40] Joint Committee for Guides in Metrology, "Evaluation of Measurement Data – Guide to the Expression of Uncertainty in Measurement," Sèvres, France, 2008.

Manuscript received 7 June 2026; Revised 13 August 2026; Accepted 19 October 2026; Available online 29 October 2026
Digital Object Identifier (**DOI**): https://doi.org/10.35882/jeeemi.v8i4.1828
Copyright © 2026 by the authors. This work is an open-access article and licensed under a Creative Commons Attribution-ShareAlike 4.0 International License (CC BY-SA 4.0)

[41] B. N. Kyle and D. W. McNeil, "Autonomic arousal and experimentally induced pain: A critical review of the literature," *Pain Res. Manag.*, vol. 19, no. 3, pp. 159–167, 2014, doi: 10.1155/2014/536859.
[42] S. Sugimine, S. Saito, and T. Takazawa, "Normalized skin conductance level could differentiate physical pain stimuli from other sympathetic stimuli," *Sci. Rep.*, vol. 10, no. 1, p. 10950, 2020, doi: 10.1038/s41598-020-67936-0.
[43] P. Kyriacou and others, "Pain assessment using physiological responses/markers in different types of pain: a scoping review," *NPJ Digit. Med.*, vol. 9, no. 1, p. 64, 2025, doi: 10.1038/s41746-025-02241-6.
[44] M. S. A. Rani, M. N. F. Norrrahim, V. F. Knight, N. M. Nurazzi, K. Abdan, and S. H. Lee, "A Review of Solid-State Proton–Polymer Batteries: Materials and Characterizations," *Polymers (Basel).*, vol. 15, no. 19, 2023, doi: 10.3390/polym15194032.

Author Biography



Wahmisari Priharti received the B.Sc. (Hons.), M.Sc., and Ph.D. degrees in Applied Physics from Universiti Kebangsaan Malaysia (UKM). She joined the School of Electrical Engineering, Telkom University, Indonesia, as a lecturer in 2018. His current research interests include biomedical imaging, low-power electronics, sensors and instrumentation, electronics for radiation systems, and machine learning. She also integrates applied physics and electronic system design to address environmental problems such as waste management and water purification.



Husneni Mukhtar received her PhD in the Doctoral School of Electronics, Microelectronics, and Photonics from Université de Strasbourg, France (2018). She began her career as a lecturer and currently supervises the Advanced Biomedical Intelligent Engineering Laboratory in the School of Electrical Engineering at Telkom University, Indonesia. Her primary interests include image-processing instrumentation for industrial inspection, biomedical analysis, nanometrology, and 3D optical profilers. She also implements instrumentation and control in other applications.



Dien Rahmawati has been a lecturer in the School of Electrical Engineering at Telkom University since 2018. She received her bachelor's degree in electronics and instrumentation from Gadjah Mada University, Indonesia, and her master's degree in electrical engineering from Bandung Institute of Technology, Indonesia. She is currently a PhD candidate in the School of Engineering at the University of Wollongong, Australia. Her research interests include assistive technology, imaging, computer vision and deep learning.



Nur Hidayah Ahmad is a Senior Lecturer in the Department of Physics, Faculty of Science, Universiti Teknologi Malaysia (UTM) and a member of the Advanced Optical Materials Research Group (AOMRG). She holds a PhD in Physics from Universiti Malaysia Terengganu. Her work focuses on the development of cellulose-based biopolymer electrolytes, proton batteries, sustainable bioplastics, and bioactive glass materials, with applications in energy storage, environmentally friendly packaging, and advanced functional materials.

Manuscript received 7 June 2026; Revised 13 August 2026; Accepted 19 October 2026; Available online 29 October 2026
Digital Object Identifier (**DOI**): https://doi.org/10.35882/jeeemi.v8i4.1828
Copyright © 2026 by the authors. This work is an open-access article and licensed under a Creative Commons Attribution-ShareAlike 4.0 International License (CC BY-SA 4.0)